Discover Sustainability

Research

Synthesis of novel Fe-BiOCl based nanosheets assembled rod (FBC-NSR)-based photoactive materials: an effective photodegradation of antibiotics

Muskan Walia[1] · Neetu Talreja[2,3] · Divya Chauhan[4] · Mohammad Ashfaq[5]

Received: 15 May 2024 / Accepted: 21 August 2024
Published online: 27 September 2024

Abstract
Fe-incorporated BiOCl-nanosheet assembled rods (FBC-NSR) based photoactive materials were synthesized using a simple sol–gel process to degrade tetracycline (TC) pharmaceuticals compound (PCs) under solar irradiation. The as-prepared FBC-NSR-based photoactive materials were characterized using various characterization techniques including scanning electron microscopy (SEM), energy dispersive X-ray spectroscopy (EDX), X-ray diffraction (XRD), diffuse reflectance spectroscopy (DRS), photoluminescent (PL) spectroscopic analysis, and Fourier transform infrared spectroscopy (FT-IR). The structural changes were observed upon doping of Fe metals within the FBC-NSR-based photoactive materials. Intriguingly, the band gap value decreased from ~ 1.81 eV to ~ 1.29 eV with increasing the amount of Fe metals (0.5 g, and 1.0 g) within the FBC-NSR named as FBC-NSR-2 and FBC-NSR-3-based photoactive materials, respectively. The lower band gap value favors the photodegradation of environmental pollution. The synthesized FBC-NSR-3 shows the highest degradation ~ 97% and ~ 72.1% at 1 mg/L and 10 mg/L TC antibiotic, respectively. The photodegradation was higher at pH 10, indicating •OH radicals play a major role in the photodegradation of TC molecules. PL spectra confirm the higher oxygen vacancy, improved transfer of electrons, and separation efficiency of photo-induced electron hole-pairs, thereby high photodegradation efficiency. Therefore, the preparation of FBC-NSR-based photoactive materials is simple, cost-effective, and promising semiconductor materials for the removal of environmental pollution.

Keywords Bismuth · Iron · Tetracycline · Nanosheets · Photoactive materials · Pollution · Semiconductors

1 Introduction

Pharmaceuticals compounds (PCs) are chemical compounds used for the treatment diagnosis, and prevention of diseases. Approximately, eighty types of PCs including antibiotics are found in water bodies. PCs mainly consist of complex molecular combinations containing mainly cyclic compounds [1–3]. A class of PCs, especially antibiotics, are widely used for the treatment of bacterial infections in humans and animals. A wide range of antibiotics are available, among them

✉ Neetu Talreja, neetutalreja99@gmail.com; ✉ Mohammad Ashfaq, mohdashfaqbiotech@gmail.com | [1]Department of Chemistry, & University Centre for Research & Development (UCRD), Chandigarh University, Gharaun, Mohali 140413, Punjab, India. [2]Faculty of Science and Technology, Department of Science, Alliance University, Bengaluru 562106, Karnataka, India. [3]Centre of Excellence For Advanced Material Synthesis and Centre of Excellence For Sophisticated Testing & Instrumentation Centre, Alliance University, Bengaluru 562106, Karnataka, India. [4]Department of Drinking Water and Sanitation, Ministry of Jal Shakti, 1208-A, Pandit Deendayal Antyodaya Bhawan, CGO Complex, Lodhi Road, New Delhi 110003, India. [5]Department of Biotechnology & University Centre for Research & Development (UCRD), Chandigarh University, Gharaun, Mohali 140413, Punjab, India.

tetracycline (TC) is a broad-spectrum antibiotic that effectively treats bacterial infectious diseases. TC consists of four rings in its structure, due to closed ring structure it is difficult to degrade [4–6]. Additionally, TC molecules are not completely consumed by the human or animal body, thereby entering into the environment through excretion and contaminating soil and water resources. TC molecules are easily adsorbed onto the surface of soil, sediment, and sludge because of their polarity and ionic compounds. Moreover, continued exposure to TC molecules significantly decreases the fertility of the soil and develops antibiotic resistance, thereby adverse effects on aquatic animals and human health [7–12]. Therefore, there is a necessity to remove/degrade TC molecules from the water system.

Several processes such as adsorption, bioremediation, membrane technology, coagulation, and photocatalysis are available to remove environmental contamination including TC molecules from wastewater. Among them, photocatalysis is one of the important processes to degrade organic contaminates like TC molecules from wastewater. Photocatalysis has been widely used for the past decades as it utilizes the ultimate source of energy, "solar energy". The utilization of solar power for wastewater treatment is a step towards sustainable development [13–15]. However, to trap the solar energy solar active catalyst/photoactive material is required to initiate the process. The valence electron can absorb photo radiation and get excited to move into the conduction band, which can finally degrade organic compounds into CO_2 and H_2O [16, 17]. Several photoactive-based materials such as transitional metal chalcogenide (TMDs) (MoS_2, $MoSe_2$, $MoTe_2$, WS_2, and WSe_2), C_3N_4, BN, MXene, graphene, graphene oxide, black phosphorus, Bi_2O_3, $BiVO_4$, Bi_2WO_6, and bismuth oxyhalides (BiOX) (X = I, Cl, and Br) based semiconductor materials have been used to degrade different environmental pollutants [7, 18–24]. Among all of them, Bi-based compounds are attracted due to their small band gap and large pore size distribution. Moreover, the incorporation of metals/non-metals within the Bi-based compounds might tune the band gap, thereby significantly improving the photodegradation ability. Several studies have been reporting the applicability of Bi-based catalysts for the photodegradation of PCs. BiOX and their oxide have also undergone some modifications like metallic and non-metallic doping to tune the band structure or to improve the mechanical strength of photoactive [25, 26]. Metallic (Fe, Cu, Zn, etc.,) doping might improve the strength and decrease the band gap of Bi-based oxides. Fe metal easily incorporates with other materials like metallic/non-metallic composite including BiOX, and has a strong potential to conduct oxidation–reduction processes, adjustable crystal sizes, economic value, and lack of toxicity. Moreover, Fe metal has the potential to prolong the life span of electron–hole separation by delaying electron–hole recombination. Additionally, Fe can effectively degrade TC molecules by exploiting the TC molecules to form chelates with particular bivalent metal ions, especially Fe (II), Mg (II), and Ca (II) [27–31]. In this context, Fe metal doping on bismuth-based compounds significantly improves the degradation of organic pollutants, ultimately high degradation ability.

This study explains the synthesis of Fe-incorporated BiOCl-nanosheet assembled rods (FBC-NSR) based photoactive materials using a facile co-precipitation process for the degradation of TC molecules. The in-situ doping of the Fe metals within the FBC-NSR skeleton significantly changes the morphology and decreases the band gap value, subsequently high degradation ability. The synthesized FBC-NSR-based photoactive agent was characterized by using several techniques including scanning electron microscopy (SEM), energy dispersive spectroscopy (EDS), X-ray diffraction (XRD), photoluminescent (PL) spectroscopic analysis, Fourier transform infrared spectroscopy (FT-IR), and diffused reflectance spectroscopy (DRS). The synthesized FBC-NSR-based photoactive materials were tested against TC molecules, which show higher photodegradation ability compared with Fe-incorporated FBC-NSR-based materials. The innovation of the FBC-NSR-based photoactive materials is the facile and cost-effective synthesis process for the removal of TC molecules. The Fe and Bi used in the FBC-NSR have distinct roles. Bi have dual roles, (1) provide exceptional visible region absorption, and (2) exhibit low band gap value. Fe metals have dual roles, (1) decrease the band gap value, and (2) modulate the structure like nanosheets assembled rods, thereby improving photoactive activity. The Fe metal doping within the BiOCl significantly improved the photoactive performance by slowing the rate of photorecombination. Moreover, Fe metals give more reactive sites and oxygen defects, thereby high photoactive ability.

2 Materials and methods

2.1 Chemicals

Bismuth oxide (Bi_2O_3), hydrochloric acid (HCl), ferric chloride ($FeCl_3$), sodium hydroxide (NaOH), ethylene diamine-tetra-acetic acid (EDTA), isopropyl alcohol (IPA), hydrogen peroxide (H_2O_2) and p-benzoquinone (BQ) and ethanol (C_2H_5OH) were purchase from SRL Chemicals, India. TC molecule was procured from Hi-media, India. The high purity grades chemicals and reagents were used in this study and solutions were prepared in deionized (DI) water.

2.2 Synthesis of FBC-NSR-based photoactive materials

FBC-NSR-based photoactive materials were synthesized using a simple co-precipitation process. Briefly, 3.8 g of the Bi_2O_3 was dissolved in 50 mL of DI containing HCl using stirring for 60 min at 60 ℃ to produce a homogenous solution of BiOCl. Approximately 1 g of $FeCl_3$ was dissolved in the 50 mL DI water using a constant stirring process at 100 rpm for 30 min at room temperature (~ 25 ℃) in a separate beaker to prepare a homogenous solution of the $FeCl_3$. Next, a homogenous solution of $FeCl_3$ was mixed into the BiOCl solution and stirred at 100 rpm for 2 h at 80 ℃ to produce a $FeCl_3$-BiOCl solution. 6 M NaOH was prepared in 100 mL DI water. The prepared NaOH solution was added drop-by-drop into $FeCl_3$-BiOCl solution and the solution was continuously stirred at 100 rpm for 2 h at room temperature (~ 25 ℃) to produce Fe-incorporated BiOCl-based nanosheets assembled rods (FBC-NSR-3) based photoactive materials. The prepared FBC-NSR-3-based photoactive material was washed several times using C_2H_5OH and DI water. Next, the washed FBC-NSR-3-based photoactive material was dried at 80 ℃ for 24 h to achieve powder of FBC-NSR-3, used for further analysis. Similarly, some FBC-NSR without Fe metals, and using 0.5 g of Fe metals, named FBC-NSR-1, and FBC-NSR-2, respectively were also prepared for assessment purposes. Figure 1 shows the schematical illustration of the various steps involved in the synthesis of FBC-NSR-based photoactive materials and their application. The FBC-NSR-based photoactive materials are synthesized by using a sol–gel process that has nanosheet-assembled nanorods. The sol–gel process mainly involves dissolving precursor (Bi) and Fe metals in a solution followed by hydrolysis and condensation reaction using NaOH, which forms FBC-NSR. Moreover, the incorporation of Fe^{+3} ions into the BiOCl might be tuned structural changes mainly the formation of nanosheets assembled nanorods. Additionally, Fe metals influence the nucleation and growth processes that promote smaller crystals. The incorporation of Fe metals also tuned electronic structure, enhanced charge carrier separation, and reduced band gap value, which significantly improved photocatalytic application.

2.3 Photocatalytic test analysis

The prepared with different Fe metals amounts and without Fe-based FBC-NSR based photoactive agent was used to determine the photoactive degradation efficiency of the TC molecules by using a solar simulator (Xenon lamp, 8000 K, 35 W). Briefly, 200 mL of various concentrations (1, 5, and 10 mg/L) of TC molecules was filled in a photocatalytic glass reactor. Next, 200 mg of the prepared FBC-NSR-based photoactive materials were added to the photocatalytic reactor and kept for 30 min in the dark. The temperature (~ 25 ℃) of the glass-photocatalytic reactor was maintained throughout the process. The samples were collected at different time exposures (-30, 0, 5, 10, 15, 20, 30, 30, 40, 50, and 60 min) of solar irradiation. Likewise, concentration study various pH (3, solution, and 10), and scavenger effects of 10 mg/L of TC molecules were used to determine the photodegradation ability of TC molecules. For ascertaining

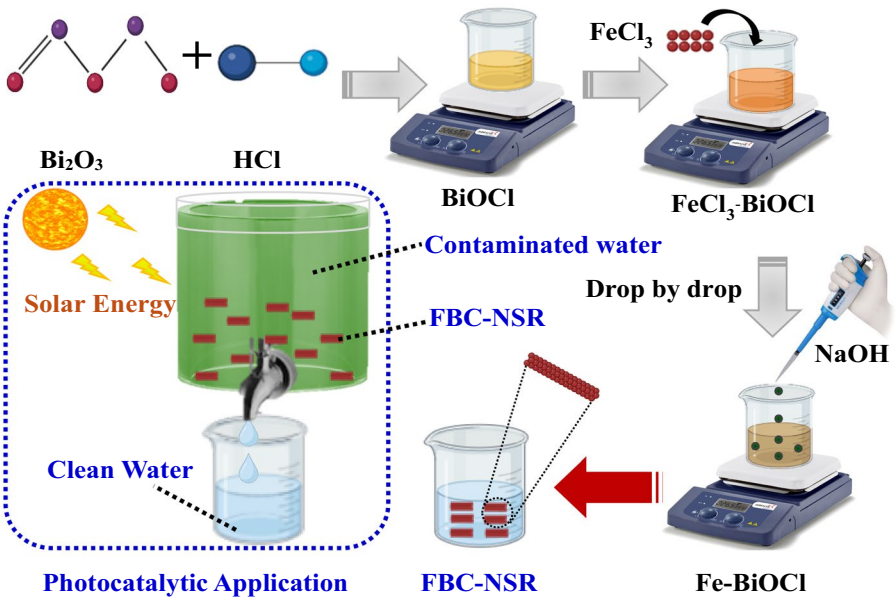

Fig. 1 A schematical illustration of the various steps involved in the synthesis of FBC-NSR-based photoactive materials and their application

H_2O_2 and scavenger's effects of FBC-NSR-based photoactive materials, EDTA, IPA, and BQ were used in radical capture tests to scavenge h^+, hydroxyl radical (·OH), and superoxide radical ($\cdot O_2^-$), respectively. The collected samples were analyzed using a UV–visible spectrophotometer (Thermo Scientific Evolution 2600).

3 Characterization of the FBC-NSR

The synthesized FBC-NSR-based photoactive materials with different amounts of Fe metals were characterized by using different techniques like scanning electron microscopy (SEM), energy dispersive X-ray spectroscopy (EDX), X-rays diffraction (XRD), diffuse reflectance spectroscopy (DRS), Fourier transform infrared spectroscopy (FT-IR), and photoluminescent (PL) spectroscopic analysis. The morphology of the different Fe metals-based FBC-NSR-based photoactive materials was observed using SEM (JEOL-JSM-IT 500). The elemental analysis and elemental mapping were observed using EDX analysis. The crystalline size and crystallographic indices of the synthesized FBC-NSR-based photoactive materials were analyzed using XRD spectroscopy with Cu K α radiation (Kα = 1.541 A°). PL emission spectra were measured by using Shimadzu 6000 RF with an excitation wavelength of 350 nm. The band gap value of the prepared FBC-NSR-based photoactive materials was determined by using DRS analysis and calculated using a Tauc plot.

4 Results and discussion

4.1 SEM analysis

Figure 2 shows the SEM images of the FBC-NSR-1 (without Fe metal loading) and different amounts of Fe metals incorporated in FBC-NSR-based photoactive materials. Figure 2a-a[1] shows the SEM images of the FBC-NSR-1-based photoactive material at higher and lower magnifications. The SEM images show the micron-sized cuboidal structures with tetrahedron shape at both ends. The rough surface and porous texture of the surface of FBC-NSR-1-based photoactive material. Interestingly, micron-sized FBC-NSR-1 entangles each other to form a flower-like structure (Fig. 2a[1]). Figure 2b-b[1] shows the SEM images of FBC-NSR-2-based photoactive material at higher and lower magnifications. The SEM images show the rough rod-like structure of FBC-NSR-2. The rough surface and some nanosheets were observed in the higher magnification SEM images of FBC-NSR-2 (Fig. 2b[1]). Figure 2c-c[1] shows the rod-like structure of the FBC-NSR-3-based photoactive materials. Interestingly, rough, and nanosheet-assembled rods were observed to attribute Fe metals to help in the formation of nanosheets. Upon increasing the amount of Fe metals within the FBC-NSR-3-based photoactive materials, nanosheets are assembled and form a rod-like structure, which might provide a more active site for the exposure of TC molecules. Furthermore, the incorporation of Fe metals substantially changes the morphology of FBC-NSR-3 aided advantages to tune the band gap value, thereby high photodegradation ability, we will revisit this aspect in the subsequent section.

Figure 3 shows the elemental analysis and mapping of the FBC-NSR-based photoactive materials. Figure 3a shows the elemental analysis of FBC-NSR-1-based photoactive material. The presence of Bi, O, and Cl confirms the synthesis of BiOCl. Figure 3b shows the elemental analysis of FBC-NSR-3-based photoactive material. The presence of Fe, Bi, O, and Cl confirms that the nanosheet-assembled rods are made up of Fe-BiOCl. Figure 3c shows the elemental mapping of FBC-NSR-3-based photoactive material. The elemental mapping confirms the uniform distribution of Fe within the FBC-NSR-based photoactive material.

4.2 XRD analysis

Figure 4 shows the XRD analysis of the prepared different Fe metal-incorporated FBC-NSR-based photoactive materials. The XRD spectra of the FBC-NSR-1 show the diffraction peaks at 2θ position of 24.70, 25.90, 27.06, 32.7, 33.48, 36.8, 40.26, 46.41, 48.67, and 54.81 attributed tetragonal phase of BiOCl (JCPDS No-06–0249) [32, 33]. Similar peaks were also observed in the prepared FB-NSR-based photoactive materials. Moreover, two new diffraction peaks at 2θ position of 30.6 and 33.61 were observed in FBC-NSR-based photoactive agents attributed to a cubic phase of Fe_3O_4, which confirms

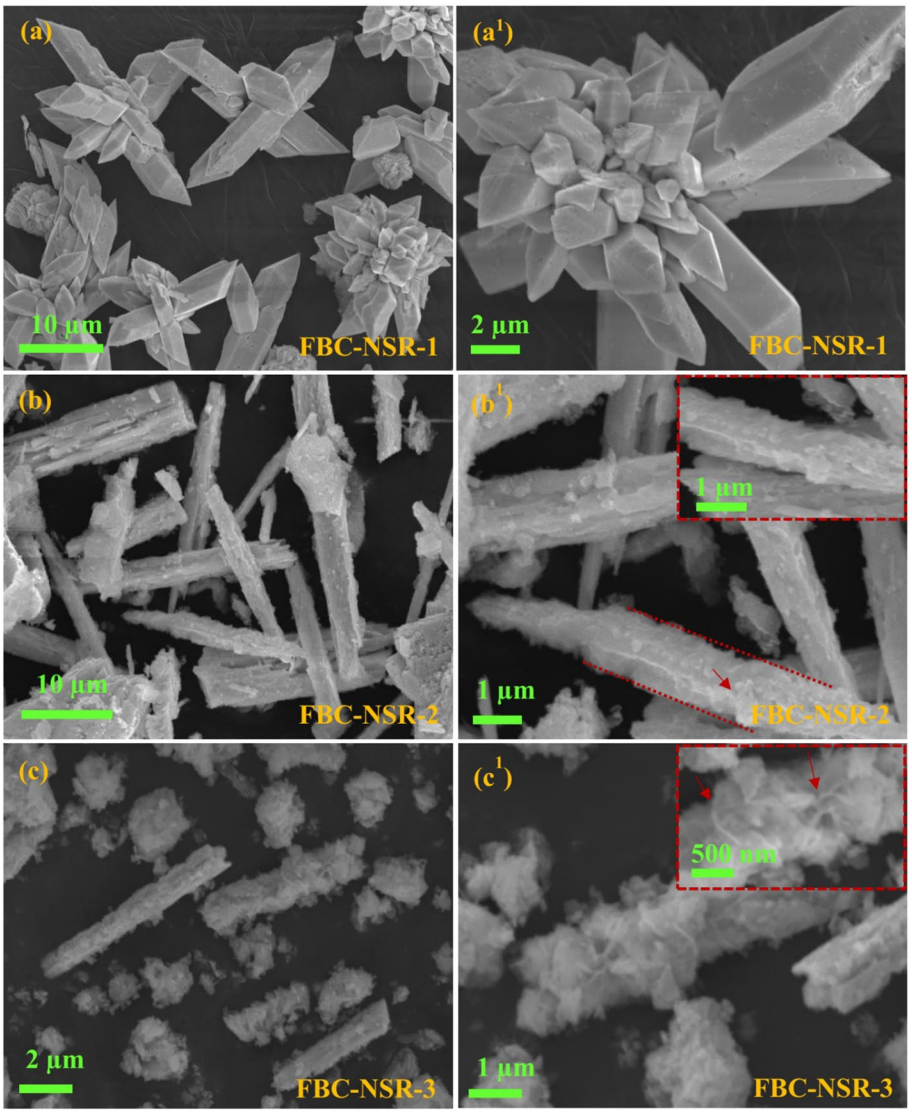

Fig. 2 SEM images of the different photoactive materials. **a**-**a**[1] FBC-NSR-1, **b**-**b**[1] FBC-NSR-2, and **c**-**c**[1] FBC-NSR-3

the synthesis of FBC-NSR (JCPDS No- 74–0748) [34]. Moreover, the changes in the dominating faces at (101) and (110) were observed due to the formation of nanosheets, which are assembled into rod-like structures, which was confirmed from the SEM images. The changes in the dominating faces and formation of nanosheets significantly improved the exposure of TC molecules [35], thereby high photoactive activity. The high crystallinity of FBC-NSR-3-based photoactive materials is due to the stabilizing effects of Fe^{3+} ions on the BiOCl lattice. The charges and ionic radius of Fe^{3+} ions are like those of Bi^{3+}, which allow Fe^{3+} ions to substitute on the BiOCl lattice without any considerable distortion, thereby a stable and ordered crystalline structure. Furthermore, Fe^{3+} ions can act as nucleation sites during the sol–gel process, which increase the smaller grain size or uniform crystal growth and improves crystallinity [36, 37]. The smaller grains size and high crystallinity might be improved photocatalytic activity of the FBC-NSR-based photoactive materials, discuss later in the manuscript.

4.3 FTIR analysis

Figure 5 shows the FTIR spectra of the different FBC-NSR-based photoactive materials. As depicted in the figure, the characteristic peaks were observed at 530 and 1389 cm^{-1}. The peak at 530 and 1389 cm^{-1} were assigned to be Bi-O and Bi-Cl, respectively, which confirm the synthesis of FBC-NSR-1. The new peaks at 525 and 633 cm^{-1} were observed in the sample of FBC-NSR-3 attributed to Fe and Fe–O, which confirm the Fe metal doping within the FBC-NSR-1-based photoactive. Additionally, the shifting of a peak at 1389–1525 cm^{-1} is mainly due to the incorporation of Fe metals. These

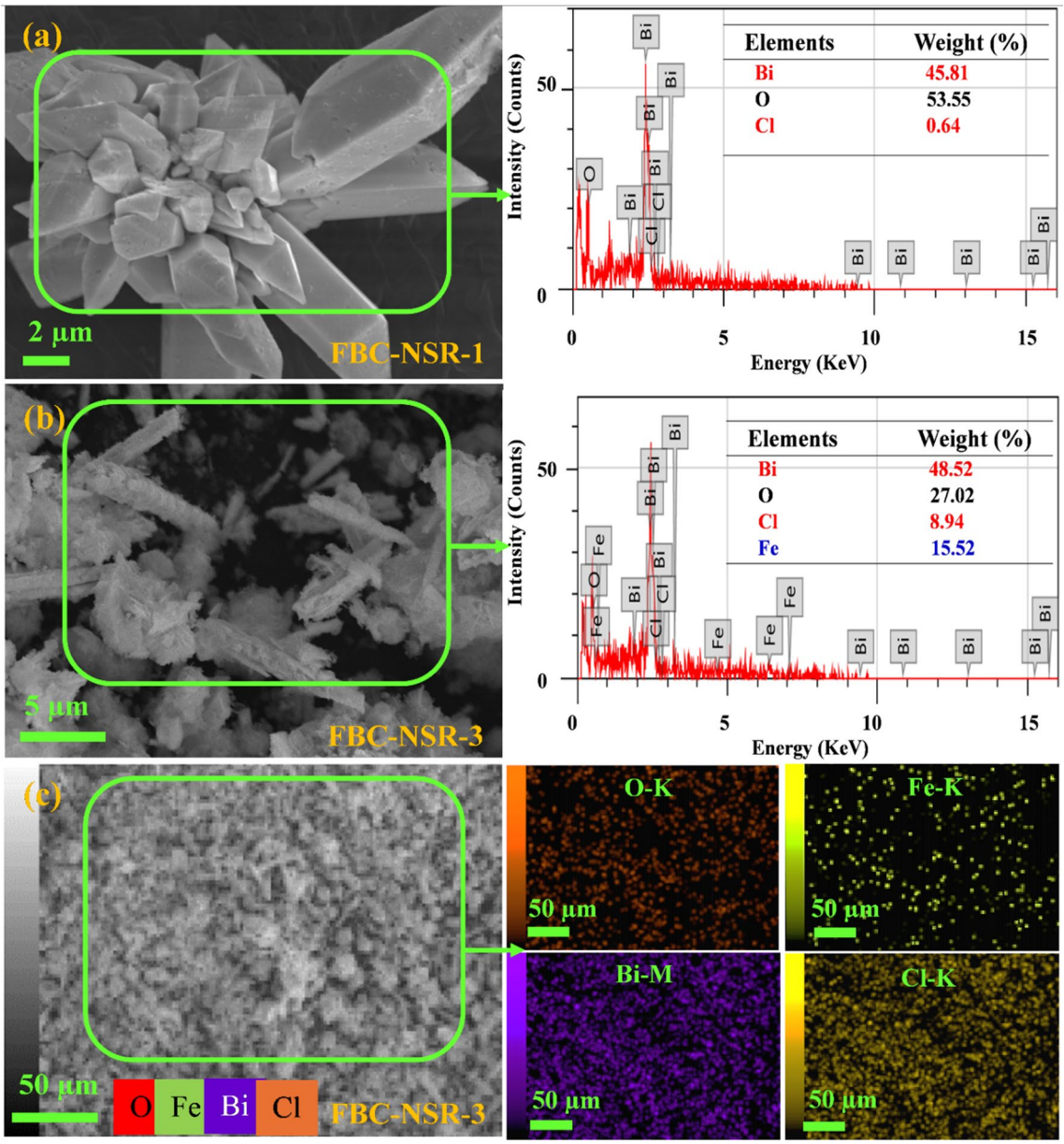

Fig. 3 Elemental analysis and mapping of the different FBC-NSR-based photoactive materials. **a**, **b** elemental analysis, and **c** elemental mapping

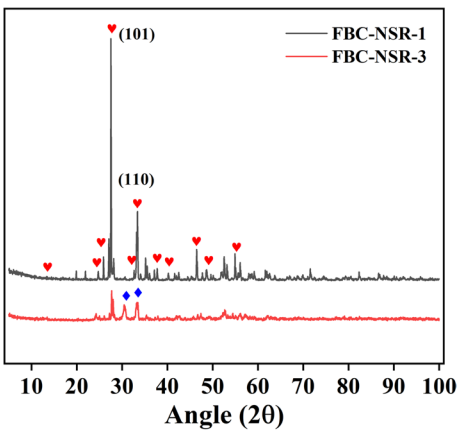

Fig. 4 XRD spectra of the different Fe metals incorporated FBC-NSR-based photoactive materials

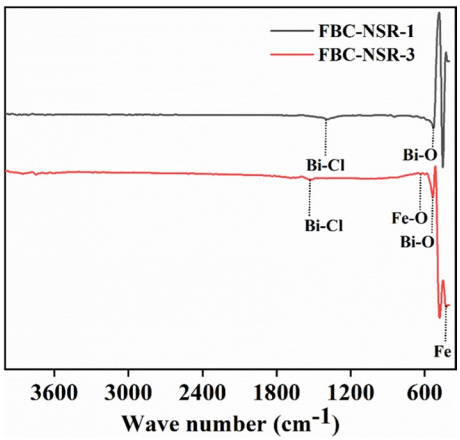

Fig. 5 FTIR Spectra of the different FBC-NSR-based photoactive materials

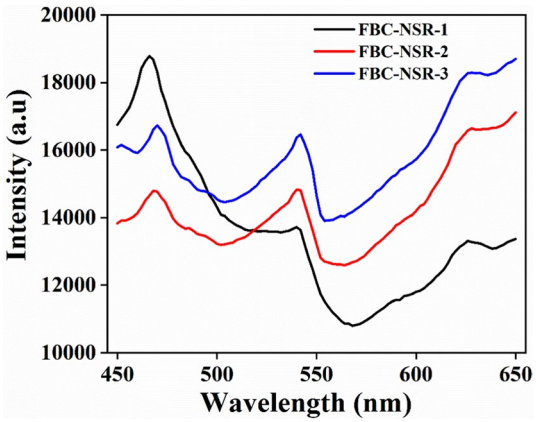

Fig. 6 PL emission spectra of the different FBC-NSR-based photoactive materials

characteristic peaks observed in the FBC-NSR-1 and FBC-NSR-3 confirm the synthesis of photoactive materials, which was also confirmed from EDX, and XRD analysis.

4.4 Optical properties

4.4.1 PL spectroscopic analysis

The PL emissions spectra of different FBC-NSR-based photoactive materials were determined at an excitation wavelength of 350 nm to understand the charge separation and photogenerated charge carriers at the surface of FBC-NSR. Figure 6 shows the PL emissions spectra of the different FBC-NSR-based photoactive materials. As depicted from the figure, the major emission was observed at 466 nm wavelength, while the minimal emission was at 540 nm wavelength in the FBC-NSR-1-based photoactive. Interestingly, upon the incorporation of Fe metals within the FBC-NSR-1, major emission was observed at 540 nm-wavelength. Moreover, increasing the Fe metal content from (0.5–1.0 g) intensity of the emission peak at 540 nm-wavelength significantly improved attributed structural changes, which is confirmed by SEM images. The higher intensity in the PL emissions spectrum mainly depends on the particle size and oxygen defects. The smaller particle size has higher oxygen vacancy and greater excitation formation, thereby high intensity of PL spectra [38–40]. The data indicates that the optical properties were significantly improved by the incorporation of Fe metals within the FBC-NSR-based photoactive materials. The Fe metals incorporation within the FBC-NSR-based photoactive materials significantly enhances the transfer of electrons and separation efficiency of photo-induced electron hole-pairs of Fe metal incorporated FBC-NSR-based photoactive [41, 42], thereby high photodegradation efficiency, discussed later in the manuscript.

4.4.2 DRS analysis

Figure 7 shows the band gap values of the prepared different FBC-NSR-based photoactive materials. The band gap values of the different FBC-NSR-based photoactive materials were determined by DRS spectroscopy and calculated using Tauc plots. The optical band gap value has been read as the intercept of the plot, according to the Tauc Plots. Figure 7a shows the band gap value of FBC-NSR-1-based photoactive materials. As depicted in the figure, the calculated band gap value was observed at ~1.81 eV. Figure 7b shows the band gap value of the FBC-NSR-2-based photoactive material. As depicted from the figure, the calculated band gap value decreases from ~1.81 to ~1.36 eV upon incorporation of Fe metals. Figure 7c shows the band gap values of FBC-NSR-3-based photoactive materials. As depicted from the figure, upon increasing Fe metals from 0.5 to 1.0 g in FBC-NSR-3-based photoactive materials, the band gap value significantly decreases from ~1.36 to ~1.29 eV due to structural changes upon incorporation of Fe metals within the FBC-NSR-based photoactive materials, which was earlier conform from SEM images. Fe metals loading within the FBC-NSR-1-based photoactive materials might decrease the band gap values which might be beneficial for the photodegradation ability of TC molecules.

Figure 7d shows the optical properties of the different FBC-NSR-based photoactive materials. As depicted from the figure, photon adsorption capacity was up to 560 nm, whereas upon incorporation of Fe metals adsorption capacity was significantly improved up to 800 nm attributed to continued adsorbed light, thereby high photodegradation of TC molecules, discussed later in the manuscript. Moreover, no adsorption edges were observed upon incorporation of Fe metals within the FBC-NSR-based photoactive materials mainly due to Fe metallic characteristics [7, 43, 44].

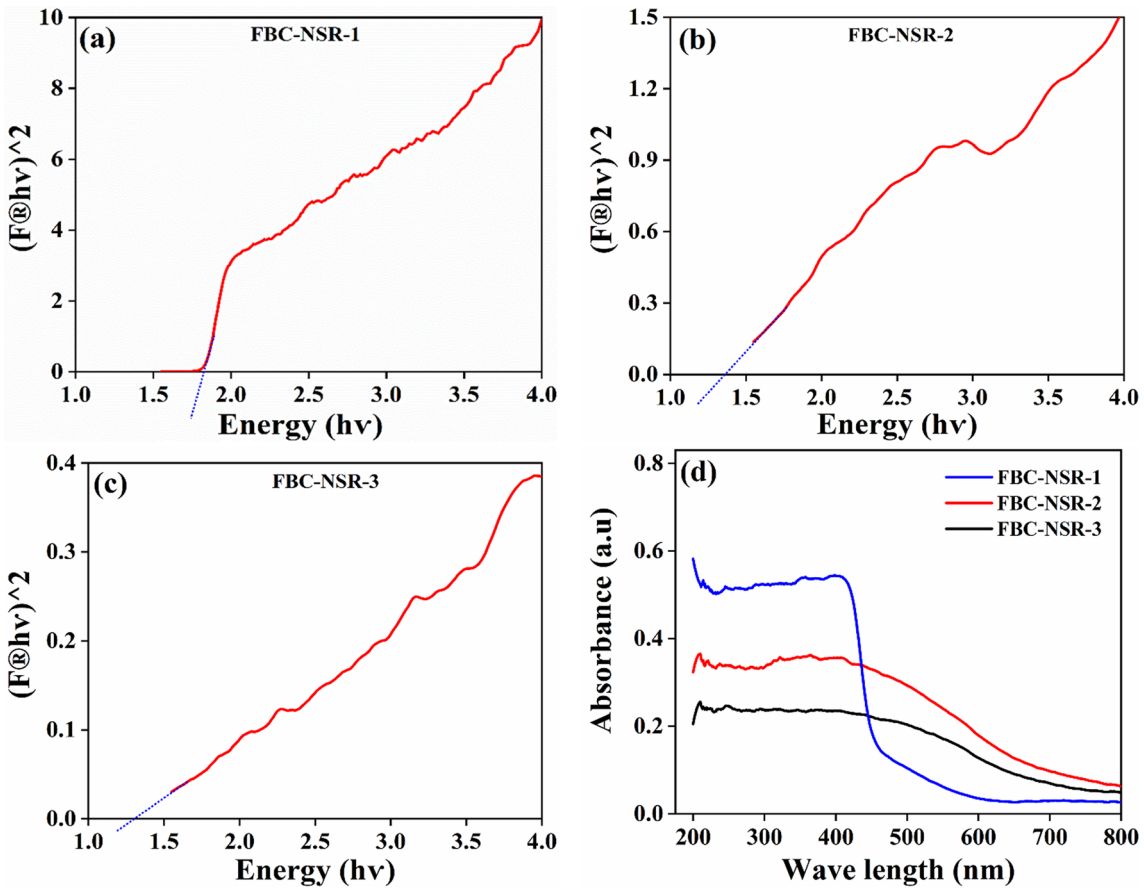

Fig. 7 Band gap value and adsorption spectra of the different FBC-NSR-based photoactive materials. **a**–**c** band gap value, and **d** optical properties

4.5 Photodegradation test assay

Figure 8 shows the photodegradation test assay of the different FBC-NSR-based photoactive materials against TC molecules. Figure 8a shows different metal amounts based on FBC-NSR-based photoactive materials at 10 mg/L of TC molecules. As depicted from the figure, photodegradation of the TC molecules increased with increasing the loading of Fe metals within the FBC-NSR-based photoactive materials. The least photodegradation efficiency of ~28.4% was observed using FBC-NSR-1-based photoactive materials (without Fe loading), whereas the highest photodegradation efficiency of ~72.1% was observed using FBC-NSR-based photoactive materials. The incorporation of Fe metals within the FBC-NSR-based photoactive materials significantly changes the morphology, which was confirmed from SEM images. The sheet-like structure assembled and formed of rods-like structure, which significantly increased the active site, thereby the highest photodegradation efficiency. Therefore, the highest Fe-loading FBC-NSR-3-based photoactive materials were used for further experiments.

Figure 8b shows the UV-VIZ spectra of TC at 10 mg/L of TC molecules using FBC-NSR-3-based photoactive materials. As depicted from the figure, the intensity of the TC peak decreased with increasing the irradiation time from 0 to 60 min, attributed to the effective degradation of TC with time. The minimum intensity of peaks/higher photodegradation was observed at 60 min of exposure to solar irradiation.

Figure 8c shows the degradation of different concentrations of the TC molecules using FBC-NSR-3. As depicted from the figure, upon increasing the concentration of TC molecules from 1 to 10 mg/L, the photodegradation efficiency of the FBC-NSR decreases from ~97% to ~72.1%, which shows the efficiency of photoactive at lower concentration of TC molecules. The degradation was found to be ~69%, ~72%, and ~97% for 10, 5 and 1 mg/L, respectively. The higher

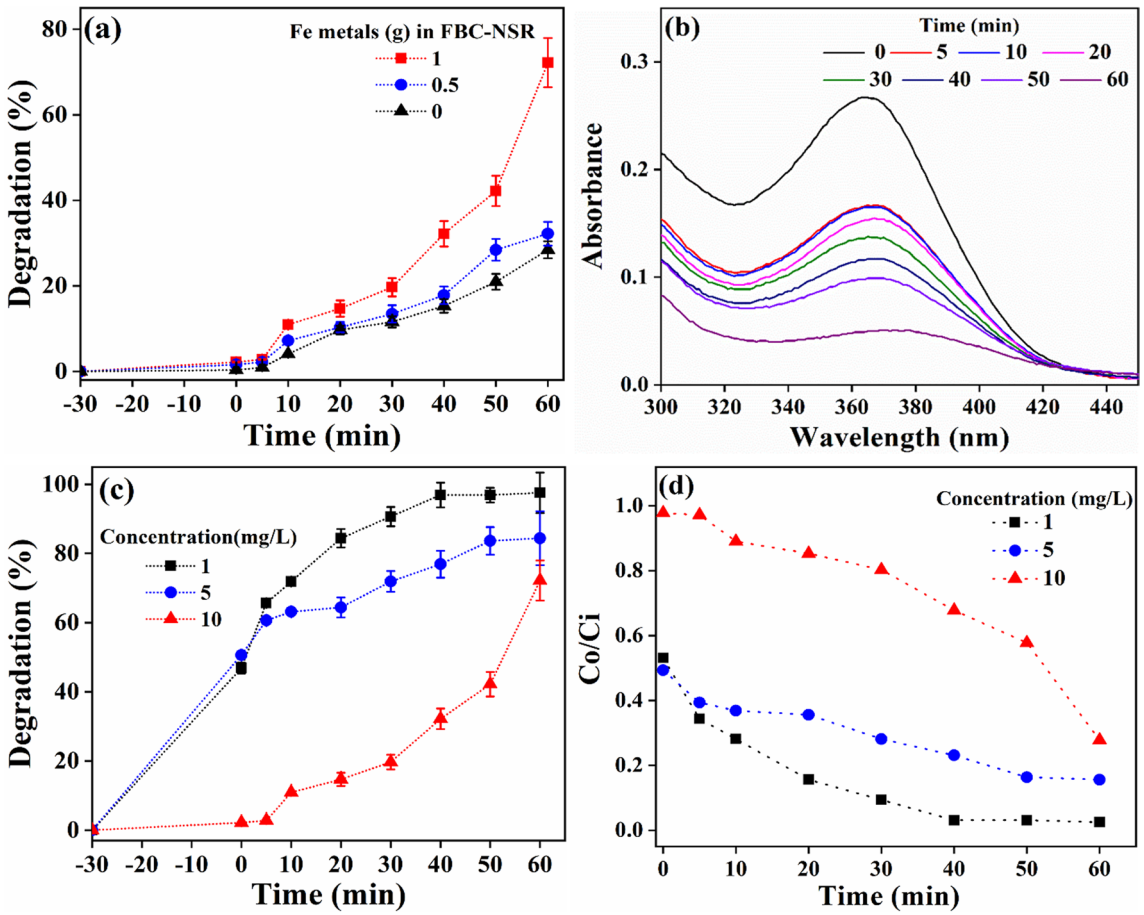

Fig. 8 Photodegradation of TC molecules using different FBC-NSR-based photoactive materials. **a** different Fe metals loaded FBC-NSR, **b** UV-VIZ spectra of TC molecules at 10 mg/L at different time intervals, **c** different concentrations of TC molecules and **d** Dimensionless concentration as a function of deterioration time at different concentrations

degradation of TC molecules at lower concentrations is due to the greater availability of active FBC-NSR surface, which can be easily accessible by the TC molecules, thereby high photodegradation efficiency. Contrary, relatively lesser availability of the active surface of FBC-NSR at higher concentrations of the TC molecules. The superior photodegradation ability of the FBC-NSR-based photoactive materials is mainly due to the formation of nanosheets-assembled rod-like structures that have high surface roughness. Several studies have suggested that the nanosheets assembled structured and high roughness of the photoactive materials significantly improved the active surface that increases the adsorption of photoelectrons, subsequently, accelerating the change transfer, thereby high photodegradation efficiency [45–47].

The dimensionless concentration as a function of deterioration time is displayed in the figure (Fig. 8 (d)) Over time, the deterioration increases for different TC concentrations due to the dissociated TC molecule, the highest degradation is observed at 1 mg/L of TC concentration. More dissociated ion concentration of TC results in increased TC degradation efficiency. Table 1. Shows the different photoactive materials for the degradation of TC antibiotics. The data shows that the prepared FBC-NSR-3-based photoactive materials have comparable degradation of TC molecules.

4.6 Effect of pH on TC degradation

Figure 9a shows the photoactive degradation of TC molecules at different pH of 10 mg/L of TC molecules. The photoactive degradation of TC molecules demonstrates a significant dependence on pH conditions. As depicted in the figure, the photodegradation efficiency of the FBC-NSR-based photoactive materials increased with increasing the pH of TC molecules. The least photodegradation ~ 33.3% of the TC molecules underwent at pH 3, attributed to photodegradation efficiency decrease in an acidic environment. Moreover, the photodegradation of TC molecules using FBC-NSR-based photoactive materials significantly improved upon changing the pH environment from acidic to neutral. Additionally, photodegradation efficiency increased with the increasing pH of the TC molecules from neutral to basic (pH 10). The highest photodegradation ~ 93.8% of TC molecules was observed at pH 10 after 60 min of solar irradiation. This emphasizes how basic pH values, especially pH 10, have a positive impact on the process of photodegradation of TC molecules. Additionally, about ~ 84% of the photodegradation happened in the first 20 min of exposure to solar light, suggesting that the FBC-NSR-based photoactive materials accelerated the pace of disintegration.

Figure 9b shows the scavenger effect of the TC molecules by using different scavengers. The maximum degradation (100%) of TC molecules was achieved by using H_2O_2 in TC molecules attributing •OH radicals play an important role in the degradation of TC molecules. The degradation of TC molecules significantly reduces upon incorporating IPA and EDTA within the TC molecules. The IPA competes with the available •OH radicals, since fewer •OH radicals are available to degrade TC molecules, thereby lowering the degradation of TC molecules. The EDTA decreases the quantity of charge carriers that can decrease the generation of •OH radicals, which lowers the degradation of TC molecules. The incorporation of BQ within the TC molecules also decreases the degradation of TC molecules, as BQ scavenges O_2•−, which also reduces the amount of reactive oxygen species (ROS) that are available to degrade TC molecules [57, 58]. The data suggests that the •OH radicals have significant roles in the degradation of TC molecules.

Figure 9c shows the recyclability test assay of FBC-NSR-3-based photoactive materials using 10 mg/L of TC molecules. The prepared FBC-NSR-3-based photoactive materials effectively degrade TC molecules up to five consecutive cycles.

Table 1 Different photoactive materials for the degradation of TC antibiotics

S. No	Photoactive materials	Synthesis process	Degradation (%)	Exposure time (min)	Refs.
1	$MnFe_2O_4$-BiOI	Green synthesis	76.02	200	[48]
2	BiOCl-CeO_2	Hydrothermal	80	120	[49]
3	BiON/$BiOCl_{0.9}I_{0.1}$	Hydrolysis	88	25	[50]
4	Fe_3O_4-BiOCl-BiOI	Solvothermal	89	80	[51]
5	BiOCl-TiO_2	Solvothermal	82	180	[52]
6	BiOI-BiOBr	Solvothermal	91.92	90	[53]
7	BiOI-MIL-125	Hydrothermal	80	240	[54]
8	$BiVO_4$	Hydrothermal	72	240	[55]
9	BiOCl-$Bi_2Ti_2O_7$ nanorods	Electrospinning	90	120	[56]
10	FBC-NSR-3	Sol–gel	72.1	60	This study

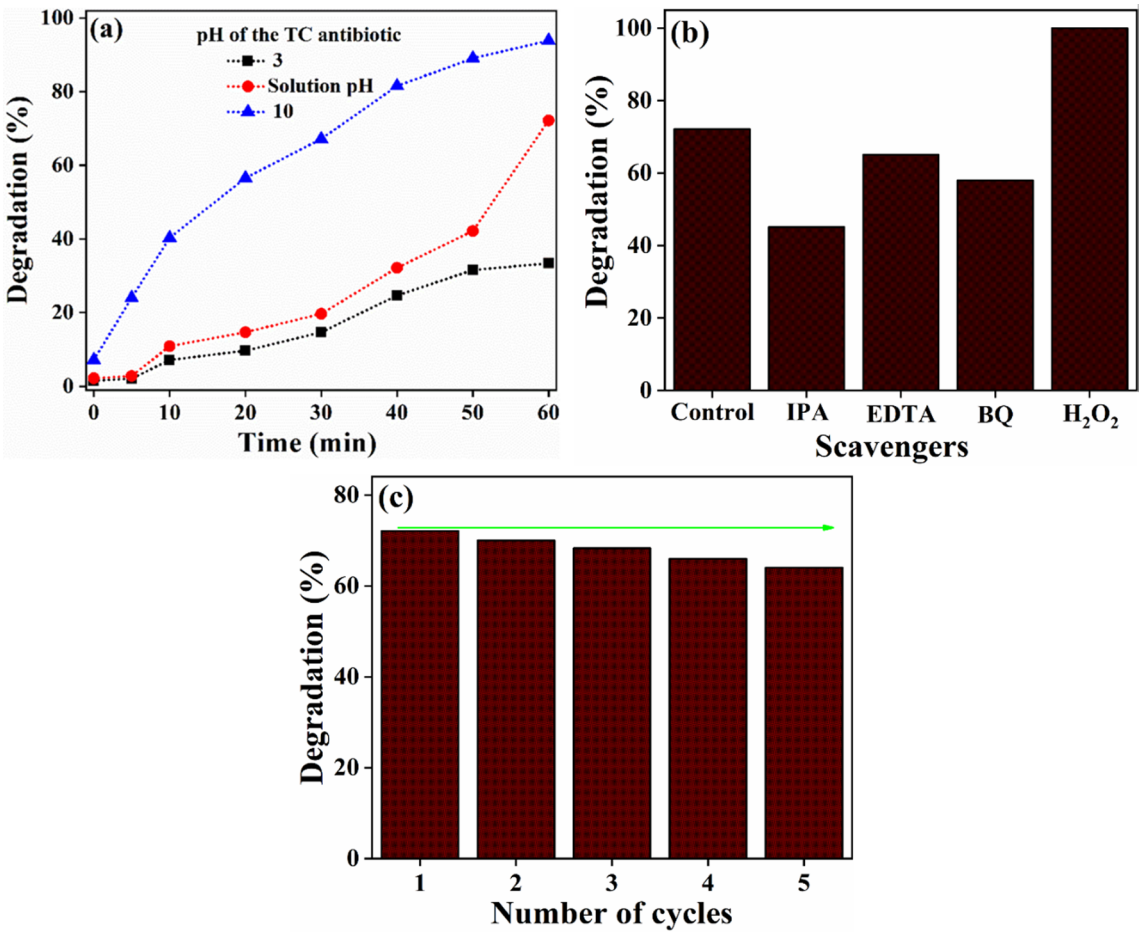

Fig. 9 Photodegradation of TC molecules at 10 mg/L by using FSC-NSR-3-based photoactive materials. **a** different pH of TC molecules, **b** scavenger's effects, and **c** recyclability test

Moreover, marginal changes in the degradation of TC molecules were observed up to five cycles attributed to the excellent reusability of FBC-NSR-3-based photoactive materials.

4.7 Plausible mechanism of the TC degradation

The photodegradation mechanism seems to be closely related to the kinetics of protonation and deprotonation of TC molecules. TC molecules acquire a negative charge in alkaline pH environments, which increases the density of anions, mainly •OH radicals. This increased anion density, particularly at pH 10, encourages the production of •OH radicals, which are essential for propelling the processes involved in photodegradation [59–61]. The prepared FBC-NSR-based photoactive materials highlight the significant influence of pH on the photodegradation of TC molecules, with basic pH conditions being more favorable for effective degradation, mainly because of increased production of •OH radicals.

Figure 10 shows the probable mechanism of FBC-NSR-based photoactive materials. The FBC-NSR-based photoactive material is exposed to solar irradiation, eventually, the generation of photoelectrons, leaving the holes behind. The FBC-NSR-based photoactive materials simply trap generated photoelectrons, leading to the separation of charges. Next, these photoelectrons form superoxide radicals with adsorbed O_2 and holes react with H_2O to form $OH^{\cdot}$ radicals. The $OH^{\cdot}$ radicals react with TC to form CO_2 and H_2O. The photodegradation of TC molecules using FBC-NSR-based photoactive materials was similar to the photodegradation of Congo red [62].

$$\text{FBC} - \text{NSR} + h\nu \rightarrow e^{-} + h^{+}$$

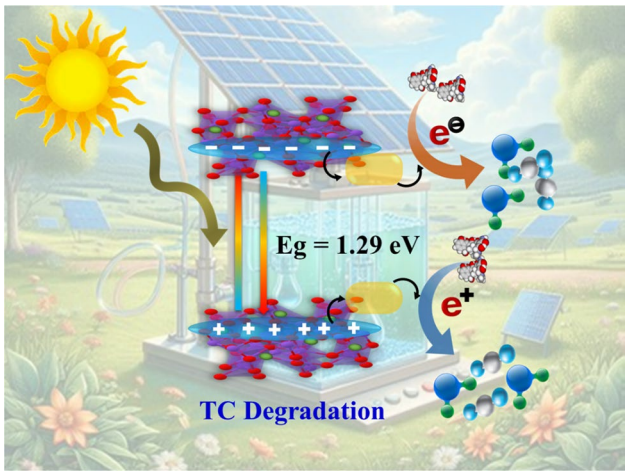

Fig. 10 Plausible mechanism of photodegradation of TC molecules using FBC-NSR-based photoactive materials

$$FBC - NSR + e^{-} \rightarrow (FBC - NSR) - e$$

$$e^{-} + O_2 \rightarrow O_2^{-}(\text{Superoxide radical})\ (\text{minor})$$

$$h^{+} + H_2O \rightarrow OH \cdot\ (\text{major})$$

$$TC + OH\cdot \rightarrow CO_2 + H_2O$$

5 Conclusion

The Fe metals incorporated FBC-NSR-based photoactive was successfully synthesized using a simple sol–gel process. The structural changes were observed upon incorporation of Fe metals within the FBC-NSR-based photoactive materials. Upon increasing the Fe metals, the formation of nanosheets which were assembled into rods-like structures, was confirmed from SEM images. Moreover, Fe metals significantly decreased the band gap values from ~ 1.89 to ~ 1.29 eV, which was the ideal band gap of any photoactive material. The higher photodegradation of ~ 97% at 1 mg/L of TC molecules was observed within 60 min of solar irradiation. Moreover, high photodegradation ability at pH attributes the •OH radicals play a major role in the photodegradation of TC molecules. Therefore, the prepared FBC-NSR-based photoactive materials might become a promising material to degrade numerous environmental pollutions.

Author contributions MW, perform all experiments and write an original draft. N.T., D.C, and M. A. analyze the data and revise the original manuscript.

Data availability The data/materials used in this study will be available on request from corresponding authors. Data sets generated during the current study are available from the corresponding author on reasonable request.

Declarations

Competing interests The authors declare no competing interests.

References

1. Samal K, Mahapatra S, Hibzur Ali M. Pharmaceutical wastewater as emerging contaminants (EC): treatment technologies, impact on environment and human health. Energy Nexus. 2022;6:100076. https://doi.org/10.1016/j.nexus.2022.100076.
2. Patel M, Kumar R, Kishor K, Mlsna T, Pittman CU Jr, Mohan D. Pharmaceuticals of emerging concern in aquatic systems: chemistry, occurrence, effects, and removal methods. Chem Rev. 2019;119(6):3510–673. https://doi.org/10.1021/acs.chemrev.8b00299.
3. Bindu S, Mazumder S, Bandyopadhyay U. Non-steroidal anti-inflammatory drugs (NSAIDs) and organ damage: a current perspective. Biochem Pharmacol. 2020;180:114147. https://doi.org/10.1016/j.bcp.2020.114147.
4. Chopra I, Roberts M. Tetracycline antibiotics: mode of action, applications, molecular biology, and epidemiology of bacterial resistance. Microbiol Mol Biol Rev. 2001;65(2):232–60. https://doi.org/10.1128/mmbr.65.2.232-260.2001.
5. Yousefi-Nooraie R, Mortaz-Hejri S, Mehrani M, Sadeghipour P. Antibiotics for treating human brucellosis. Cochrane Database Syst Rev. 2012;10(10):Cd007179. https://doi.org/10.1002/14651858.CD007179.pub2.
6. Zhang X, Pan Y, Wang Y, Wu T, Shao B, He Q, Zhou L, Li T, Liu S, Huang X, Liu Z. MOF derived MnFeOX supported on carbon cloth as electrochemical anode for peroxymonosulfate electro-activation and persistent organic pollutants degradation. Chem Eng J. 2024;481:148646. https://doi.org/10.1016/j.cej.2024.148646.
7. Talreja N, Ashfaq M, Chauhan D, Viswanathan MR. PVP encapsulated MXene coated on PET surface (PMP)-based photocatalytic materials: a novel photo-responsive assembly for the removal of tetracycline. Environ Res. 2023;233:116439. https://doi.org/10.1016/j.envres.2023.116439.
8. Polianciuc SI, Gurzău AE, Kiss B, Ştefan MG, Loghin F. Antibiotics in the environment: causes and consequences. Med Pharm Rep. 2020;93(3):231–40. https://doi.org/10.1538/mpr-1742.
9. Daghrir R, Drogui P. Tetracycline antibiotics in the environment: a review. Environ Chem Lett. 2013;11(3):209–27. https://doi.org/10.1007/s10311-013-0404-8.
10. Yang Q, Gao Y, Ke J, Show PL, Ge Y, Liu Y, Guo R, Chen J. Antibiotics: an overview on the environmental occurrence, toxicity, degradation, and removal methods. Bioengineered. 2021;12(1):7376–416. https://doi.org/10.1080/21655979.2021.1974657.
11. Wu S, Yi B, Lan D. Fabrication of Bi2MoO6/g-C3N4 visible-light driven photocatalyst for enhanced tetracycline degradation. J Photochem Photobiol A: Chem. 2023;444:115013. https://doi.org/10.1016/j.jphotochem.2023.115013.
12. Shabnam N, Talreja D, Ashfaq Chauhan M. Synthesis of waste derived bimetallic (Fe/ca) oxy-iodide (WD-BMOX) encapsulated with PVDF based nanosphere (WD-BMOX-P) as solar active agent: an efficient photodegradation of antibiotic. Sustain Mater Technol. 2024. https://doi.org/10.1016/j.susmat.2024.e01081.
13. Kumar R, Awino E, Njeri DW, Basu A, Chattaraj S, Nayak J, Roy S, Khan GA, Jeon BH, Ghosh AK, Pal S, Banerjee S, Rout P, Chakrabortty S, Tripathy SK. Advancing pharmaceutical wastewater treatment: a comprehensive review on application of catalytic membrane reactor-based hybrid approaches. J Water Process Eng. 2024;58:104838. https://doi.org/10.1016/j.jwpe.2024.104838.
14. Al-Nuaim MA, Alwasiti AA, Shnain ZY. The photocatalytic process in the treatment of polluted water. Chem Pap. 2023;77(2):677–701. https://doi.org/10.1007/s11696-022-02468-7.
15. Titchou FE, Zazou H, Afanga H, El Gaayda J, Ait Akbour R, Nidheesh PV, Hamdani M. Removal of organic pollutants from wastewater by advanced oxidation processes and its combination with membrane processes. Chem Eng Proc Process Intensif. 2021;169:108631. https://doi.org/10.1016/j.cep.2021.108631.
16. Pavel M, Anastasescu C, State R-N, Vasile A, Papa F, Balint I. Photocatalytic degradation of organic and inorganic pollutants to harmless end products: assessment of practical application potential for water and air cleaning. Catalysts. 2023. https://doi.org/10.3390/catal13020380.
17. Hammer NI, Sutton S, Delcamp J, Graham JD. Photocatalytic water splitting and carbon dioxide reduction. In: Chen W-Y, Suzuki T, Lackner M, editors. Handbook of climate change mitigation and adaptation. New York: Springer; 2014. p. 1–39.
18. Guo F, Li M, Ren H, Huang X, Hou W, Wang C, Shi W, Lu C. Fabrication of p-n CuBi2O4/MoS2 heterojunction with nanosheets-on-microrods structure for enhanced photocatalytic activity towards tetracycline degradation. Appl Surf Sci. 2019;491:88–94. https://doi.org/10.1016/j.apsusc.2019.06.158.
19. Singla S, Singh P, Basu S, Devi P. BiVO4/MoSe2 Photocatalyst for the photocatalytic abatement of tetracycline and photoelectrocatalytic water splitting. Mater Chem Phys. 2023;295:127111. https://doi.org/10.1016/j.matchemphys.2022.127111.
20. Wang X, Lu Q, Sun Y, Liu K, Cui J, Lu C, Dai H. Fabrication of novel p-n-p heterojunctions ternary WSe2/In2S3/ZnIn2S4 to enhance visible-light photocatalytic activity. J Environ Chem Eng. 2022;10(5):108354. https://doi.org/10.1016/j.jece.2022.108354.
21. Fatima T, Husain S, Khanuja M. Superior photocatalytic and electrochemical activity of novel WS2/PANI nanocomposite for the degradation and detection of pollutants: antibiotic, heavy metal ions, and dyes. Chem Eng J Adv. 2022;12:100373. https://doi.org/10.1016/j.ceja.2022.100373.
22. Talreja N, Afreen S, Ashfaq M, Chauhan D, Mera AC, Rodríguez CA, Mangalaraja RV. Bimetal (Fe/Zn) doped BiOI photocatalyst: an effective photodegradation of tetracycline and bacteria. Chemosphere. 2021;280:130803. https://doi.org/10.1016/j.chemosphere.2021.130803.
23. Ashfaq M, Talreja N, Chauhan D, Rodríguez CA, Mera AC, Mangalaraja RV. A novel bimetallic (Fe/Bi)-povidone-iodine micro-flowers composite for photocatalytic and antibacterial applications. J Photochem Photobio B: Biol. 2021;219:112204. https://doi.org/10.1016/j.jphotobiol.2021.112204.
24. Talreja N, Ashfaq M, Chauhan D, Mera AC, Rodríguez CA. Strategic doping approach of the Fe–BiOI microstructure: an improved photodegradation efficiency of tetracycline. ACS Omega. 2021;6(2):1575–83. https://doi.org/10.1021/acsomega.0c05398.

25. Zhang L, Li Y, Li Q, Fan J, Carabineiro SAC, Lv K. Recent advances on bismuth-based photocatalysts: strategies and mechanisms. Chem Eng J. 2021;419:129484. https://doi.org/10.1016/j.cej.2021.129484.
26. Chen P, Liu H, Cui W, Lee SC, Wang LA, Dong F. Bi-based photocatalysts for light-driven environmental and energy applications: structural tuning, reaction mechanisms, and challenges. EcoMat. 2020;2(3):e12047. https://doi.org/10.1002/eom2.12047.
27. Ghosh S, Laha D, Hajra P, Sariket D, Ray D, Baduri S, Sahoo HS, Bhattacharya C. Development of transition metal incorporated bismuth-based oxide semiconductors as potential candidates for solar assisted water splitting applications. ChemElectroChem. 2023;10(6):e202201062. https://doi.org/10.1002/celc.202201062.
28. Hu T, Li H, Du N, Hou W. Iron-doped bismuth tungstate with an excellent photocatalytic performance. ChemCatChem. 2018;10(14):3040–8. https://doi.org/10.1002/cctc.201701965.
29. Tolan DA, El-Sawaf AK, Alhindawy IG, Ismael MH, Nassar AA, El-Nahas AM, Maize M, Elshehy EA, El-Khouly ME. Effect of bismuth doping on the crystal structure and photocatalytic activity of titanium oxide. RSC Adv. 2023;13(36):25081–92. https://doi.org/10.1039/d3ra04034h.
30. Rusu A, Buta EL. The development of third-generation tetracycline antibiotics and new perspectives. Pharmaceutics. 2021. https://doi.org/10.3390/pharmaceutics13122085.
31. Wang H, Yao H, Sun P, Li D, Huang C-H. Transformation of tetracycline antibiotics and Fe(II) and Fe(III) species induced by their complexation. Environ Sci Technol. 2016;50(1):145–53. https://doi.org/10.1021/acs.est.5b03696.
32. Li L, Zhang M, Zhao Z, Sun B, Zhang X. Visible/near-IR-light-driven TNFePc/BiOCl organic–inorganic heterostructures with enhanced photocatalytic activity. Dalton Trans. 2016;45(23):9497–505. https://doi.org/10.1039/C6DT01091A.
33. Ye L, Jin X, Leng Y, Su Y, Xie H, Liu C. Synthesis of black ultrathin BiOCl nanosheets for efficient photocatalytic H2 production under visible light irradiation. J Power Sour. 2015;293:409–15. https://doi.org/10.1016/j.jpowsour.2015.05.101.
34. Tan C, Zhu G, Hojamberdiev M, Xu C, Liang J, Luo P, Liu Y. Room temperature synthesis and photocatalytic activity of magnetically recoverable Fe3O4/BiOCl nanocomposite photocatalysts. J Cluster Sci. 2013;24(4):1115–26. https://doi.org/10.1007/s10876-013-0602-3.
35. Xu Y, Shi Z, Zhang LE, Brown EMB, Wu A. Layered bismuth oxyhalide nanomaterials for highly efficient tumor photodynamic therapy. Nanoscale. 2016;8(25):12715–22. https://doi.org/10.1039/C5NR04540A.
36. Di LJ, Yang H, Xian T, Li RS, Feng YC, Feng WJ. Influence of precursor Bi3+/Fe3+ ion concentration on hydrothermal synthesis of BiFeO3 crystallites. Ceram Int. 2014;40(3):4575–8. https://doi.org/10.1016/j.ceramint.2013.08.134.
37. Xiaohong W, Wei Q, Li L, Yun G, Zhaoyang X. Photocatalytic property of nanostructured Fe3+-doped Bi2O3 films. Catal Commun. 2009;10(5):600–4. https://doi.org/10.1016/j.catcom.2008.11.001.
38. Zulkiflee A, Khan MM, Khan A, Khan MY, Dafalla HDM, Harunsani MH. Sn-doped BiOCl for photoelectrochemical activities and photocatalytic dye degradation under visible light. Heliyon. 2023;9(11):e21270. https://doi.org/10.1016/j.heliyon.2023.e21270.
39. Mani R, Vivekanandan K, Vallalperuman K. Synthesis of pure and cobalt (Co) doped SnO2 nanoparticles and its structural, optical and photocatalytic properties. J Mater Sci: Mater Electron. 2017;28(5):4396–402. https://doi.org/10.1007/s10854-016-6067-z.
40. Liqiang J, Yichun Q, Baiqi W, Shudan L, Baojiang J, Libin Y, Wei F, Honggang F, Jiazhong S. Review of photoluminescence performance of nano-sized semiconductor materials and its relationships with photocatalytic activity. Solar Energy Mater Solar Cells. 2006;90(12):1773–87. https://doi.org/10.1016/j.solmat.2005.11.007.
41. Xu L, Yan P, Li H, Ling S, Xia J, Qiu J, Xu Q, Li H, Yuan S. Metallic Bi self-doping BiOCl composites: synthesis and enhanced photoelectrochemical performance. Mater Lett. 2017;196:225–9. https://doi.org/10.1016/j.matlet.2017.03.008.
42. Shang J, Zhao B, Gao Y, Chen H, Wang X. Enhanced electricity generation in photoelectrochemical cell using Sn-doped BiOCl photoanode. J Mater Sci: Mater Electron. 2020;31(16):13939–46. https://doi.org/10.1007/s10854-020-03953-z.
43. Xu J, Feng B, Wang Y, Qi Y, Niu J, Chen M. BiOCl decorated NaNbO3 nanocubes: a novel p-n heterojunction photocatalyst with improved activity for ofloxacin degradation. Front Chem. 2018. https://doi.org/10.3389/fchem.2018.00393.
44. Jiang R, Wu D, Lu G, Yan Z, Liu J, Zhou R, Nkoom M. Fabrication of Fe3O4 quantum dots modified BiOCl/BiVO4 p-n heterojunction to enhance photocatalytic activity for removing broad-spectrum antibiotics under visible light. J Taiwan Inst Chem Eng. 2019;96:681–90. https://doi.org/10.1016/j.jtice.2019.01.010.
45. Guo X, Wu D, Long X, Zhang Z, Wang F, Ai G, Liu X. Nanosheets-assembled Bi2WO6 microspheres with efficient visible-light-driven photocatalytic activities. Mater Charact. 2020;163:110297. https://doi.org/10.1016/j.matchar.2020.110297.
46. Coto M, Troughton SC, Knight P, Joshi R, Francis R, Kumar RV, Clyne TW. Optimization of the microstructure of TiO2 photocatalytic surfaces created by plasma electrolytic oxidation of titanium substrates. Surf Coat Technol. 2021;411:127000. https://doi.org/10.1016/j.surfcoat.2021.127000.
47. Najafidoust A, Kazemi Hakki H, Alinezhad Avalzali H, Karimi Ashraf Bonab M. The role of diethanolamine as stabilizer in controlling morphology, roughness and photocatalytic activity of ZnO coatings in sonophotodegradation of methylene blue. Mater Res Express. 2019;6(9):096401. https://doi.org/10.1088/2053-1591/ab2a43.
48. Golrizkhatami F, Taghavi L, Nasseh N, Panahi HA. Synthesis of novel MnFe2O4/BiOI green nanocomposite and its application to photocatalytic degradation of tetracycline hydrochloride: (LC-MS analyses, mechanism, reusability, kinetic, radical agents, mineralization, process capability, and purification of actual pharmaceutical wastewater). J Photochem Photobiol A: Chem. 2023;444:114989. https://doi.org/10.1016/j.jphotochem.2023.114989.
49. Wang H, Liao B, Lu T, Ai Y, Liu G. Enhanced visible-light photocatalytic degradation of tetracycline by a novel hollow BiOCl@CeO2 heterostructured microspheres: structural characterization and reaction mechanism. J Hazard Mater. 2020;385:121552. https://doi.org/10.1016/j.jhazmat.2019.121552.
50. Yang X, Shen Q, Cao W, Xu B, Sun Y, Li C. In-situ template etching synthesis of BiON/BiOCl0.9I0.1 heterojunction for photocatalytic degradation of tetracycline. ChemPhysMater. 2024;3(1):103–10. https://doi.org/10.1016/j.chphma.2023.08.001.
51. Dang J, Guo J, Wang L, Guo F, Shi W, Li Y, Guan W. Construction of Z-scheme Fe3O4/BiOCl/BiOI heterojunction with superior recyclability for improved photocatalytic activity towards tetracycline degradation. J Alloys Compd. 2022;893:162251. https://doi.org/10.1016/j.jallcom.2021.162251.

52. Bao S, Liang H, Li C, Bai J. The synthesis and enhanced photocatalytic activity of heterostructure BiOCl/TiO2 nanofibers composite for tetracycline degradation in visible light. J Dispersion Sci Technol. 2021;42(13):2000–13. https://doi.org/10.1080/01932691.2020.1795669.
53. Ni Q, Ke X, Qian W, Yan Z, Luan J, Liu W. Insight into tetracycline photocatalytic degradation mechanism in a wide pH range on BiOI/BiOBr: coupling DFT/QSAR simulations with experiments. Appl Catal B: Environ. 2024;340:123226. https://doi.org/10.1016/j.apcatb.2023.123226.
54. Jiang W, Li Z, Liu C, Wang D, Yan G, Liu B, Che G. Enhanced visible-light-induced photocatalytic degradation of tetracycline using BiOI/MIL-125(Ti) composite photocatalyst. J Alloys Compd. 2021;854:157166. https://doi.org/10.1016/j.jallcom.2020.157166.
55. Hemavibool K, Sansenya T, Nanan S. Enhanced photocatalytic degradation of tetracycline and oxytetracycline antibiotics by BiVO(4) photocatalyst under visible light and solar light irradiation. Antibiotics. 2022. https://doi.org/10.3390/antibiotics11060761.
56. Xu Y, Lin D, Liu X, Luo Y, Xue H, Huang B, Chen Q, Qian Q. Electrospun BiOCl/Bi2Ti2O7 nanorod heterostructures with enhanced solar light efficiency in the photocatalytic degradation of tetracycline hydrochloride. ChemCatChem. 2018;10(11):2496–504. https://doi.org/10.1002/cctc.201800100.
57. Iqbal A, Saidu U, Sreekantan S, Ahmad MN, Rashid M, Ahmed NM, Danial WH, Wilson LD. Mesoporous TiO2 implanted ZnO QDs for the photodegradation of tetracycline: material design, structural characterization and photodegradation mechanism. Catalysts. 2021. https://doi.org/10.3390/catal11101205.
58. Li X, Xiong J, Gao X, Ma J, Chen Z, Kang B, Liu J, Li H, Feng Z, Huang J. Novel BP/BiOBr S-scheme nano-heterojunction for enhanced visible-light photocatalytic tetracycline removal and oxygen evolution activity. J Hazard Mater. 2020;387:121690. https://doi.org/10.1016/j.jhazmat.2019.121690.
59. Song J, Yuan X, Sun M, Wang Z, Cao G, Gao K, Yang C, Zhang F, Dang F, Wang W. Oxidation of tetracycline hydrochloride with a photoenhanced MIL-101(Fe)/g-C3N4/PMS system: synergetic effects and radical/nonradical pathways. Ecotoxicol Environ Saf. 2023;251:114524. https://doi.org/10.1016/j.ecoenv.2023.114524.
60. Liu X, Zhou Y, Sun S, Bao S. Study on the behavior and mechanism of NiFe-LDHs used for the degradation of tetracycline in the photo-fenton process. RSC Adv. 2023;13(45):31528–40. https://doi.org/10.1039/D3RA05475F.
61. Zhao C, Pelaez M, Duan X, Deng H, O'Shea K, Fatta-Kassinos D, Dionysiou DD. Role of pH on photolytic and photocatalytic degradation of antibiotic oxytetracycline in aqueous solution under visible/solar light: kinetics and mechanism studies. Appl Catal B: Environ. 2013;134–135:83–92. https://doi.org/10.1016/j.apcatb.2013.01.003.
62. Tariq A, Ali SI, Akinwande D, Rizwan S. Efficient visible-light photocatalysis of 2D-MXene nanohybrids with Gd3+- and Sn4+-codoped bismuth ferrite. ACS Omega. 2018;3(10):13828–36. https://doi.org/10.1021/acsomega.8b01951.